



# *In-situ* SEM investigation on stress-induced microstructure evolution of austenitic stainless steels subjected to cavitation erosion and cavitation erosion-corrosion

Ye Tian<sup>a,b</sup>, Hang Zhao<sup>a,b</sup>, Rui Yang<sup>a,b</sup>, Xiaomei Liu<sup>a,b</sup>, Xiuyong Chen<sup>a,b,c,\*</sup>, Jiahao Qin<sup>a,b</sup>, André McDonald<sup>d</sup>, Hua Li<sup>a,b,c</sup>

<sup>a</sup>Zhejiang Engineering Research Center for Biomedical Materials, Cixi Institute of Biomedical Engineering, Ningbo Institute of Materials Technology and Engineering, Chinese Academy of Sciences, Ningbo 315201, China

<sup>b</sup>Key Laboratory of Marine Materials and Related Technologies, Zhejiang Key Laboratory of Marine Materials and Protective Technologies, Ningbo Institute of Materials Technology and Engineering, Chinese Academy of Sciences, Ningbo 315201, China

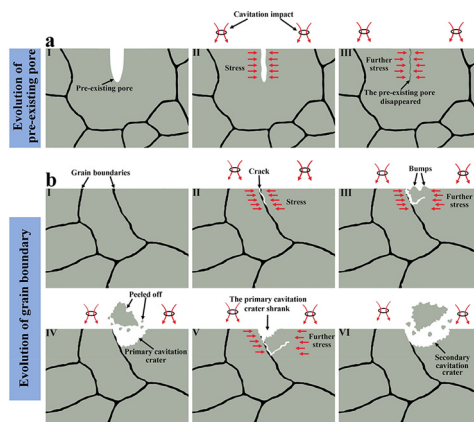
<sup>c</sup>Center of Materials Science and Optoelectronics Engineering, University of Chinese Academy of Sciences, Beijing 100049, China

<sup>d</sup>Department of Mechanical Engineering, University of Alberta, Edmonton AB T6G 1H9, Canada

## HIGHLIGHTS

- Stress-induced phase transformation was observed in 304 SS during cavitation erosion.
- A possible exacerbation mechanism of corrosion on cavitation erosion was suggested.
- Cavitation erosion did not start at the pre-existing pores (formed during casting).
- The evolution of cavitation erosion crack was studied via *in-situ* SEM observation.

## GRAPHICAL ABSTRACT



## ARTICLE INFO

### Article history:

Received 13 October 2021

Revised 1 December 2021

Accepted 7 December 2021

Available online 8 December 2021

### Keywords:

Austenitic stainless steel

Cavitation erosion

Cavitation erosion-corrosion

*In-situ* SEM observation

Microstructure evolution

## ABSTRACT

This study investigated the effect of stress on the microstructure evolution of austenitic stainless steels (316L SS and 304 SS) subjected to cavitation erosion and cavitation erosion-corrosion. Results show that continuous accumulation of stress of austenitic stainless steels at the early stage of cavitation erosion was observed from the samples tested in deionised water (DIW) but not in artificial seawater (ASW), which is due to stress release induced by ASW. In addition, a stress-induced phase transformation from austenite to martensite during the cavitation erosion tests in both DIW and ASW was observed in 304 SS, but not in 316 SS. Furthermore, primary cavitation craters formed during the cavitation erosion were not expanded directly but shrank first and then expanded due to re-accumulation of stress. More importantly, this study reports for the first time that pre-existing pores are not initiation points of cavitation erosion damage, possibly because of the ductility of austenitic stainless steels, which resulted in continuous shrinkage of the pores caused by the accumulated stress. Our findings provide new insights into understanding the

\* Corresponding author at: Zhejiang Engineering Research Center for Biomedical Materials, Cixi Institute of Biomedical Engineering, Ningbo Institute of Materials Technology and Engineering, Chinese Academy of Sciences, Ningbo 315201, China.

E-mail address: [chenxiuyong@nimte.ac.cn](mailto:chenxiuyong@nimte.ac.cn) (X. Chen).

Stress failure mechanisms of austenitic stainless steels subjected to cavitation erosion, which will inform the development of high-performance cavitation erosion-resistant materials.  
 © 2021 The Author(s). Published by Elsevier Ltd. This is an open access article under the CC BY-NC-ND license (<http://creativecommons.org/licenses/by-nc-nd/4.0/>).

## 1. Introduction

Cavitation erosion is a typical failure mode that frequently occurs on engineering components, such as pumps impellers, hydraulic turbines, and ship propellers, through which high-speed fluid passes [1–5]. Shock waves and microjets generated by the collapse of the cavitation bubble cause cavitation erosion [6–8]. Cavitation erosion accelerates the degradation of the components exposed to high-speed fluid, severely reducing their service lifetime [9,10]. Thus, the development of high-performance cavitation erosion resistant materials is urgently needed to extend service life and reduce maintenance costs. Meanwhile, comprehensive understanding of the failure mechanisms of cavitation erosion is foundational to the design of high-performance anti-cavitation erosion materials. Therefore, studies on cavitation erosion failure mechanisms have resulted in an active area of research [11,12]. It has been reported that, at the early stage of cavitation erosion, the surface of materials can generate a large number of dislocations to absorb energy produced by cavitation erosion [13,14]. However, some dislocations are unstable and easily move to adjacent grain boundaries. As a result, the dislocations are blocked by the grain boundaries, which can cause grain strain and stress concentration at the grain boundary [15,16]. In the subsequent cavitation erosion process, cracks will be produced in the grain and/or at the grain boundary, which can be initial site of cavitation erosion [17–20]. Although researchers have observed that stress accumulation leads to the generation of cracks, thus forming the initial sites of cavitation erosion, the evolution process of these initial sites under further stress has not been studied.

Although the surface morphology of the sample after cavitation erosion can be used to infer the formation process of cavitation craters [21,22], the deduced evolution process may be inconsistent with the actual evolution process. *In-situ* scanning electron microscopy (SEM) observation is a very effective strategy for studying the failure evolution mechanism of materials [23–25]. Such as generation and propagation of fatigue microcracks in pre-corrosion AA7075-T7651 aluminium alloy [26], the relationship between crack propagation and microstructure of TC21 titanium alloy during the tensile process [27] as well as crack propagation behaviour of die-casting AlSiMgMn alloy during tensile tests [28]. Recently, we proposed an *in-situ* SEM observation and analysis route for investigating cavitation erosion failure mechanisms of thermal-sprayed coatings [29], providing direct evidence of the effect of pre-existing defects on cavitation erosion failure of coatings. Nevertheless, there is still a paucity of knowledge on the mechanisms of the cavitation erosion failure process.

In this paper, commonly used materials 316L stainless steel (316L SS) and 304 stainless steel (304 SS) were investigated. Specifically, the stress accumulation and release at the early stage of cavitation erosion in deionized water (DIW) and in artificial seawater (ASW) were investigated by X-ray diffraction (XRD) and SEM. More importantly, the formation and further evolution process of primary cavitation craters under cavitation in DIW and ASW were firstly studied by *in-situ* SEM observation. Meanwhile, this paper also explored the evolution process of pre-existing pores (casting defects [30–32]) in the process of stress accumulation caused by cavitation erosion. This study intends to provide a reference for the design of anti-cavitation erosion and anti-cavitation erosion-corrosion materials.

## 2. Materials and methods

Stainless steels 316L and 304, commonly used in hydraulic and marine engineering, were chosen as typical austenitic stainless steels in this study. The samples with 20 mm in diameter and 10 mm in thickness were cut from the 316L SS and the 304 SS bars with a diameter of 20 mm. The samples were ground by using 120-, 400-, 800-, 1200-, and 2000-mesh sandpapers with tap water, and then polished by 2.5  $\mu\text{m}$  and 0.25  $\mu\text{m}$  diamond polishing solution (Wuyi Hengyu Instrument Co., Ltd., China), respectively. The polished samples were ultrasonically cleaned with DIW and ethanol (Sinopharm Chemical Reagent Co., Ltd., China) for 5 min, respectively, and then dried in a vacuum oven (DZF6050, Shanghai Yiheng Scientific Instrument Co., Ltd., China) at room temperature. The ASW (NaCl: 24.53 g/L,  $\text{MgCl}_2$ : 5.20 g/L,  $\text{Na}_2\text{SO}_4$ : 4.09 g/L,  $\text{CaCl}_2$ : 1.16 g/L, KCl: 0.695 g/L,  $\text{NaHCO}_3$ : 0.201 g/L, KBr: 0.101 g/L,  $\text{H}_3\text{BO}_3$ : 0.027 g/L,  $\text{SrCl}_2$ : 0.025 g/L, NaF: 0.003 g/L) was prepared as per ASTM D1141-98 (2013) [33], and the reagents were commercially available (Sinopharm Chemical Reagent Co., Ltd., China).

The as-polished samples were electrochemically etched to analyse their metallographic structure. The electrolyte was 68% nitric acid (Sinopharm Chemical Reagent Co., Ltd., China) in DIW, and the electrolysis process was at an electrolysis voltage of 1.2 V for 60 s [34]. The samples after etching were cleaned and dried in a vacuum oven at room temperature, and then the microstructure of the samples was observed by SEM (Regulus 8230, Hitachi Manufacturing Co., Ltd., Japan).

For cavitation erosion test, the ultrasonic cavitation equipment (GBS-SCT 20A, Hangzhou Guobiao Ultrasonic Equipment Co., Ltd., China) was operated at a frequency of 20 kHz and an amplitude of 50  $\mu\text{m}$ . The temperature of the test medium was maintained at  $25 \pm 2$  °C by a cooling system. The sample was placed at 1 mm below the ultrasonic horn, and the ultrasonic horn was placed at  $23 \pm 2$  mm below the testing medium surface. The schematic diagram of the device is shown in Fig. 1. Vickers hardness (VH3300, Buehler Ltd., USA) of the sample was tested every 5 min until the cavitation time reached 45 min. All the indented sites were within 5 mm to the center of the sample. Ten points

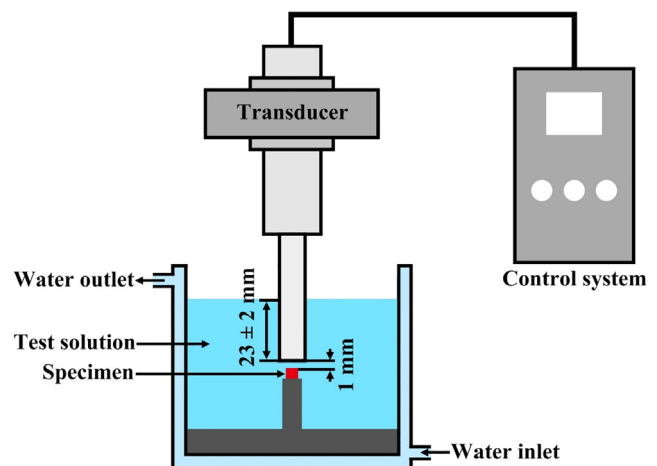


Fig. 1. Schematics of the cavitation erosion test system.

on the surface of the samples were randomly selected to measure the Vickers hardness, and the average value and error were calculated. The load was 0.2 kgf and the dwell time was 10 s for the Vickers hardness indentations. The XRD patterns of the samples exposed to 0 min, 5 min, 15 min, 30 min, and 45 min of cavitation erosion in DIW and ASW were acquired by the D8 Advance (Bruker Ltd., Germany) with a copper anode at 40 kV and 40 mA in a glancing angle of  $43.2^\circ - 45.0^\circ$  ( $2\theta$  degree) with a step size of  $0.01^\circ$ . The surface morphologies of the samples were observed by using SEM after 45 min of cavitation erosion in DIW and ASW. For the *in-situ* SEM analysis, representative regions were selected from the previous electrochemically etched sample. Abaqus 2021 Student Edition was applied to simulate the stress distribution around the pre-existing pore, and the model is shown in Fig. S1. The dynamic strain was studied by using the Johnson-Cook material constitutive law [35], and the parameters of the constitutive model are listed in Table S1.

### 3. Results and discussion

#### 3.1. Stress accumulation during cavitation erosion and its effect on phase structure and Vickers hardness

XRD patterns of the samples after cavitation erosion in DIW and ASW for different times are shown in Fig. 2A. After the first 15 min of exposure to cavitation erosion in DIW, the diffraction peak of austenite ( $\gamma$  (1 1 1)) of the 316L SS continuously moves to the left with increased cavitation erosion time. According to the Bragg equation of  $2d\sin\theta = n\lambda$  ( $n = 1, 2, 3, \dots$ ) [36], the left-shifting of the peak indicates a decrease in  $2\theta$ , and thus the interplanar spacing increases, which further indicates the accumulation of tensile stress in the sample after cavitation erosion. In addition, the tensile stress is proportional to the increment of  $2\theta$  [37,38]. However, further left-shifting of the austenite peaks of the 316L SS exposed to 30 min and 45 min of cavitation erosion is insignificant. This phenomenon may result from the release of tensile stress, which can be due to the formation of cracks on the surface (Fig. 2B: 316L, 45 mins-DIW). Furthermore, it is worth noting that the left-shifting of the austenite peak is less significant in ASW (Fig. 2A: 316L-ASW), which is quite different from what was observed in DIW. As the test conditions were consistent (except for the test medium), it is highly possible that the stress should have accumulated in the sample was released by some means. According to the surface morphologies of the 316L SS before and after cavitation erosion in DIW and ASW for 45 min (Fig. 2B), more cracks appeared on the surface of the 316L SS after being tested in ASW than that of tested in DIW. Literature reported that cracks can be induced by the combined influence of stress and corrosion, namely stress corrosion cracking [39]. Thus, the increased number of cracks may be attributed to the stress corrosion cracking. As the tensile stress was released with the generation and propagation of cracks [40,41], the left-shifting of the austenite peak of the 316L SS is not obvious after cavitation erosion in ASW. Similar results were observed from XRD patterns and surface morphologies for the 304 SS (Fig. 2). The cavitation erosion results of the 316L SS and 304 SS show that the initiation and the propagation of the cracks are more pronounced in ASW than those in DIW, indicating the negative effect of corrosion on cavitation erosion of the samples, which could further reduce the strength of the austenitic stainless steels. As cracks are also the nucleation sites of cavitation bubbles [42] and tend to hold cavitation bubbles [43], generation and propagation of the cracks could be responsible for the decreased cavitation erosion resistance of austenitic stainless steels in corrosive environments.

The 304 SS underwent stress accumulation similar to that of 316L SS during cavitation erosion in DIW, but the process of stress accumulation is quite different. For the 304 SS exposed to cavitation erosion in DIW, the overall offset of the left-shifting of the austenite peak ( $\gamma$ (1 1 1)) is  $0.046^\circ$  at 15 min (Fig. 2A), which is only 36.5% that of the 316L SS ( $0.126^\circ$ ). However, it can be considered that there is almost no difference in the amount of energy input to different samples during the cavitation erosion under the same test conditions. Thus, the reduced amount of the left-shifting of the 304 SS indicates that there can be other ways to absorb or dissipate cavitation erosion energy in 304 SS. Meanwhile, the intensity of the martensite peaks ( $\alpha'$ (1 1 0) &  $\epsilon$ (002)) in 304 SS increased with the extension of the cavitation erosion time (Fig. 3A), indicating that martensitic phases were generated. The  $\epsilon$ -martensite is usually the intermediate in the transformation from austenite to  $\alpha'$ -martensite [7]. This phenomenon is probably attributed to the stress-induced phase transformation of the austenite to the martensite [44,45]. Since martensitic transformation requires energy (such as strain energy [46,47]), the transformation process might have absorbed a considerable amount of energy, resulting in decreased stress accumulation. Therefore, the left-shifting of the austenite diffraction peak in 304 SS is less than that of the 316L SS. In addition, the intensity of the martensite peaks ( $\alpha'$ (1 1 0) &  $\epsilon$ (002)) in 304 SS after cavitation in ASW are amplified with the increase in the cavitation time as well, similar to that observed for tests conducted in DIW. To further investigate the stress-induced phase transformation, *in-situ* SEM observations were employed for the 304 SS after different cavitation erosion times in DIW (Fig. 3B). It could be clearly seen that with the extension of cavitation erosion time, the stress accumulation leads to increasingly severe deformation (highlighted by the red dotted line), which induces more martensite transformation [44,45].

In summary, the XRD results indicate that the tensile stress on the surface of the 316L SS and the 304 SS increased significantly at the beginning of the cavitation erosion test in DIW, but little change occurred during the tests in ASW. Moreover, the 304 SS exhibited a stress-induced phase transformation during cavitation erosion. The accumulation of stress and the phase transformation behaviour of the austenitic stainless steels during cavitation erosion may affect its surface Vickers hardness.

Vickers hardness of the 316L SS and the 304 SS subjected to different cavitation erosion times in DIW and ASW is shown in Fig. 4A&B. For the sample tested in DIW, the Vickers hardness of the 316L SS increased rapidly in the first 10 min (from  $201 \pm 3$  to  $239 \pm 5$ ), then slowly from 10 min ( $239 \pm 5$ ) to 35 min ( $276 \pm 18$ ), and insignificantly after 35 min (from  $276 \pm 18$  to  $274 \pm 18$ ). With increased exposure to cavitation erosion, the variation of Vickers hardness became greater across the sample, suggesting that the stress distribution on the sample surface was less uniform after exposure to cavitation erosion. For the sample tested in ASW, the Vickers hardness of 316L SS increased rapidly in the first 5 min (from  $201 \pm 3$  to  $238 \pm 8$ ), then increased slowly from 5 min ( $238 \pm 8$ ) to 20 min ( $277 \pm 10$ ), and remained relatively stable from 20 min ( $277 \pm 10$ ) to 45 min ( $284 \pm 16$ ). The Vickers hardness of the 316L SS tested in ASW increased faster than that in DIW, which only took about 20 min ( $277 \pm 10$ ) to close to the maximum value ( $288 \pm 19$ ), while it took 35 min in DIW. This result indicates that the cavitation erosion failure mechanism of the 316L SS in DIW can be different from that in ASW, which is corresponding to the difference in XRD patterns (Fig. 2A). The evolution of Vickers hardness of the 304 SS tested in DIW and ASW (Fig. 4B) is similar to that of the 316L SS. The Vickers hardness of the 316L SS and 304 SS increased continuously as the exposure time was increased, which can be attributed to the work hardening effect due to the repeated load caused by cavitation erosion [48,49]. The increase in the Vickers hardness is shown in Fig. 4C.

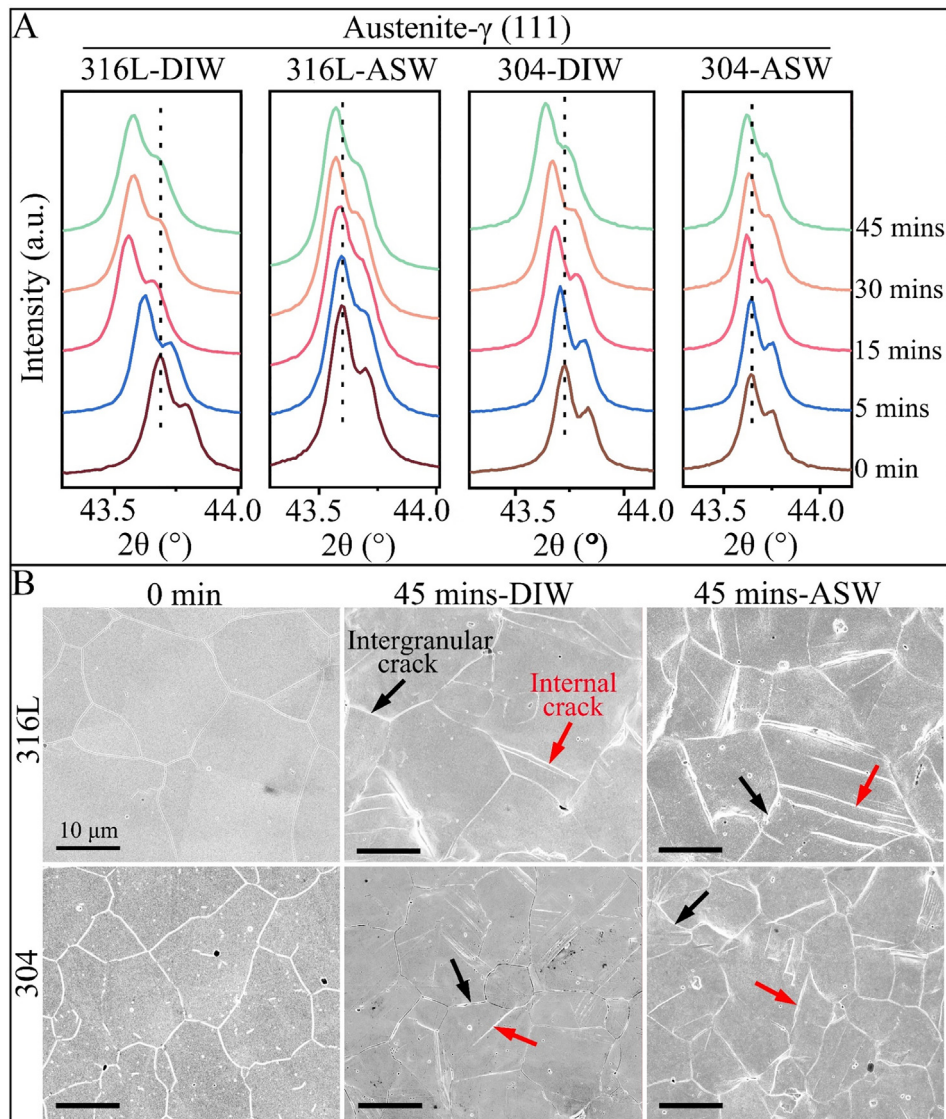


**Fig. 2.** (A) X-ray diffraction patterns of the austenite peaks of 316L SS and 304 SS with different cavitation times in DIW and ASW; (B) Surface morphologies of 316L SS and 304 SS before and after 45 min of cavitation erosion in DIW and ASW (black arrow: intergranular crack; red arrow: internal cracks). (For interpretation of the references to colour in this figure legend, the reader is referred to the web version of this article.)

After 45 min of cavitation erosion in DIW and ASW, the Vickers hardness of the 316L SS increased by 39% and 43%, while that of the 304 SS increased by 45% and 53%, respectively. The austenite to martensite transformation in the 304 SS during cavitation erosion is responsible for the higher increase in Vickers hardness compared with that of the 316L SS, as the hardness of martensite is significantly greater than that of austenite [50,51] and the 316L SS did not exhibit such phase transformation (Fig. 3A). Generally, the increased hardness is always correlated to increased yield strength and tensile strength but results in a decrease in fatigue strength. Higher hardness means more brittleness and lower fatigue strength [52], which means more energy is needed to produce cracks on the surface of the 304 SS. Therefore, the cracks on the surface of the 304 SS after 45 min of cavitation erosion were significantly less than that of the 316L SS (Fig. 2B). Fewer cracks mean fewer cavitation development sites, and this could explain why the 304 SS has higher cavitation resistance than the 316L SS (Fig. S2). In addition, typical indentation morphologies of the 316L SS and 304 SS (Fig. 4D), where the indentation mark became smaller with the increase in exposure to cavitation (from 0 to 15 min), also indicates the increase of the work hardening effect.

Although average higher Vickers hardness increased when the sample was further exposed to cavitation erosion (from 25 to 45 min, as shown in Fig. 4 A&B and Fig. S4-S7), no statistically significant difference was observed. This might be attributed to the initiation and propagation of cracks as the test time was extended, as it is well recognised that the presence of cracks in materials can reduce the Vickers hardness of the materials. On the other hand, the Vickers hardness of the samples exposed to cavitation erosion in ASW is significantly higher than those in DIW, possibly attributed to denser passivation film on the surface of the samples after cavitation erosion in ASW [53–55].

### 3.2. The effect of stress accumulation on the formation and evolution progress of crater during cavitation erosion

To further clarify the effect of stress accumulation on microstructure evolution of austenitic stainless steels subjected to ultrasonic cavitation erosion, *in-situ* SEM observation of the 316L SS and 304 SS under cavitation erosion condition in DIW were carried out (Fig. 5). For the as-etched 316L SS surface (Fig. 5A-1), the grain boundaries are clear, and the surface is free of cracks.

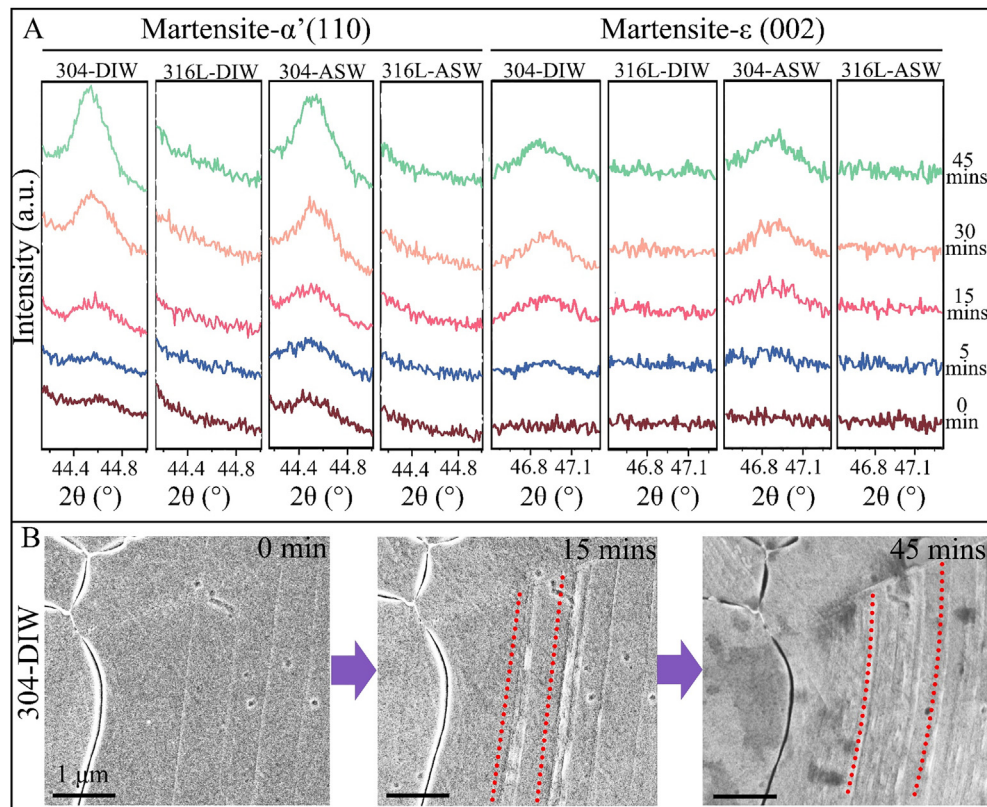


**Fig. 3.** (A) X-ray diffraction patterns of martensite peaks of 304 SS and 316L SS with different cavitation times in DIW and ASW. (B) *In-situ* SEM observation of stress-induced phase transition of 304 SS after 0 min, 15 min, and 45 min of cavitation erosion in DIW solution (red dotted lines: deformed region and martensite). (For interpretation of the references to colour in this figure legend, the reader is referred to the web version of this article.)

With the extension of the cavitation erosion times, the stress on the surface of the samples continued to accumulate (Fig. 5A-2 to A-4), causing cracks to appear on the surface and then form a cavitation crater (Fig. 5A-5). It is interesting that the cavitation crater shrunk, from 7.88  $\mu\text{m}$  (Fig. 5A-5) to 5.24  $\mu\text{m}$  (Fig. 5A-6), which is attributed to the extrusion of the surrounding grains of the cavitation crater. The *in-situ* SEM observation of the 304 SS tested in DIW (Fig. 5B) shows no cracks on grain boundaries or inside grains before cavitation erosion (Fig. 5B-1). After being tested in DIW for different cavitation erosion times, grain boundary crack was observed (Fig. 5B-2), and then the cavitation erosion craters were formed (Fig. 5B-3). The grain could absorb the cavitation erosion energy by producing a large number of dislocations at the early stage of cavitation erosion, and some of these generated dislocations easily slip to the grain boundaries and were blocked by the grain boundaries [15,16], resulting in grain boundary strain and causing the crack of the grain boundary (Fig. 5B-3). With the extension of cavitation erosion time, the inconsistent movement between the grains caused the grain boundary cracks, and then a cavitation crater was formed (Fig. 5B-3). It is worth noting that the width of the cavitation crater formed at the 75th minute of cavitation erosion was reduced from 2.81 to 1.29  $\mu\text{m}$  in the subsequent cavitation erosion process (Fig. 5B-3 to B-5). The shrinkage of the cavitation crater could be attributed to the extrusion of the grains around the cavitation crater. At the 120th minute (Fig. 5B-6), the grain reached the plastic limit, and further upward movement caused the rupture of the grain, resulting in the formation of a large secondary cavitation crater.

The *in-situ* SEM observation of the 316L SS and 304 SS at the grain boundaries subjected to cavitation erosion in ASW was also

performed (Fig. 6). The shrinking process of primary cavitation crater in ASW is similar to the results observed in DIW, but cracks (highlighted by the red arrows) appear at the bottom of the cavitation craters of the samples after cavitation erosion in ASW (Fig. 6A-5 and B-5), and the cracks widen as the cavitation erosion time increased (Fig. 6A-6 and B-6). This phenomenon was not observed in the sample after cavitation erosion in DIW (Fig. 5A-5 to A-6 and B-3 to B-6), which indicates that the corrosion caused by ASW can induce stress release and cause cracks, which are similar to the results observed in Fig. 2B.

For a better understanding of the formation and evolution progress of the cavitation crater during cavitation erosion, a schematic diagram is shown in Fig. 7. The inconsistent movement between the grains causes the stress in the grain and/or at the grain boundary, and the accumulated stress causes the deformation of the grain and/or the grain boundary. When the accumulated stress reaches the endurance limit, crack generates at the grain boundary (Fig. 7B-1) and/or in the grain (Fig. 7B-2) [56,57]. When further exposure to the cavitation erosion conditions, the crack continues to grow, accompanied by further deformation (Fig. 7C-1 and C-2). When reaching the plastic deformation limit, the grain is delaminated and detached, forming an initial cavitation crater (Fig. 7D). However, it is worth noticing that the initial cavitation crater is not expanded directly but narrowed first (Fig. 7E) and then expanded (Fig. 7F). The reduction of the initial cavitation crater is caused by the extrusion of the surrounding grains to the crater, resulting in the further accumulation of the stress. The grains at/near the initial cavitation crater can be peeled off to form a secondary cavitation crater (Fig. 7F).

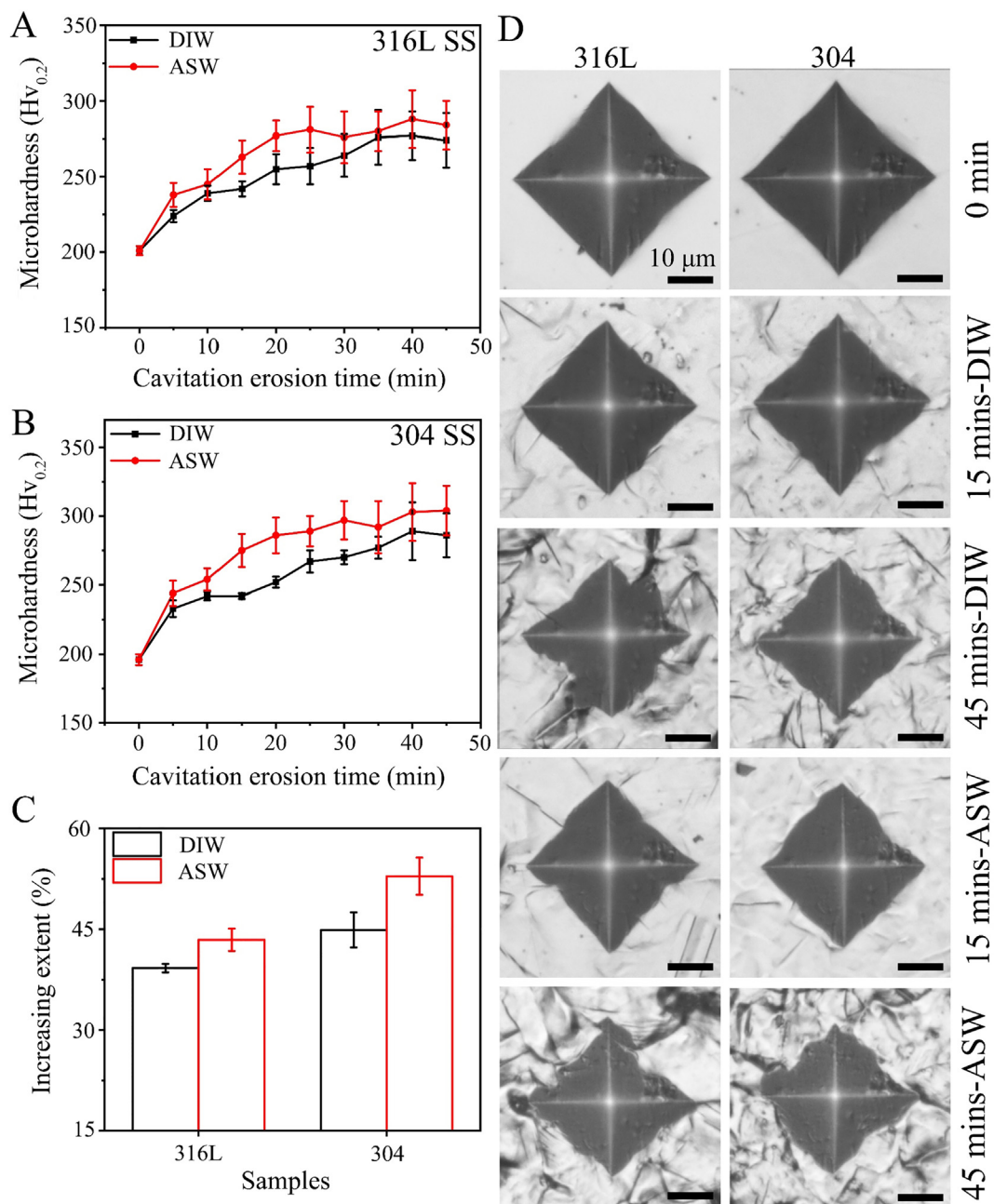


**Fig. 4.** The microhardness of the 316L SS (A) and the 304 SS (B) in DIW and ASW with different cavitation times. (C) The increase of the microhardness of 316L SS and 304 SS after 45 min cavitation erosion. (D) Typical indentation morphologies of the 316L SS and the 304 SS at different cavitation times, and more indentation morphologies and entire sample morphologies are shown in **Figs. S3-S7**.

### 3.3. The effect of stress accumulation on the evolution process of pre-existing pore during cavitation erosion

It is well known that cast alloys usually have pre-existing pores (casting defects) on the surface [58–60], and the pore defects on the surface of the materials are commonly recognised as the starting point of cavitation erosion [2]. Thus, the evolution of the pre-existing pores on the surface of austenitic stainless steels under cavitation erosion condition is worth studying. The *in-situ* SEM observation of a pre-existing pore of the 316L SS during cavitation erosion in DIW is shown in **Fig. 8A**. The pre-existing pore has a diameter of about 1.54 μm, which may be sourced from the casting process [30–32]. The pore size decreased with the increase of the cavitation erosion time (**Fig. 8A-2 to A-3**), and finally, the pore

almost disappeared (**Fig. 8A-4**) due to the continuous extrusion of the surrounding grains. The *in-situ* SEM observation of the cavitation erosion of a pre-existing pore on a 304 SS sample in DIW (**Fig. 8B**) also shows a similar microstructure evolution. The size of the pre-existing pore decreased (**Fig. 8B-2 to B-3**) with the extension of the cavitation time, and the pore was finally enclosed (**Fig. 8B-4**) by the squeezing of the grains nearby. To understand the behaviour of pre-existing pores under cavitation erosion-corrosion conditions, *in-situ* SEM observation of the pre-existing pores of the austenitic stainless steels tested in ASW was also investigated (**Fig. 8C & D**). The results show that the pore after cavitation erosion in ASW eventually disappeared (**Fig. 8C-4 & D-4**), which is similar to the evolution process of the pores tested in DIW.

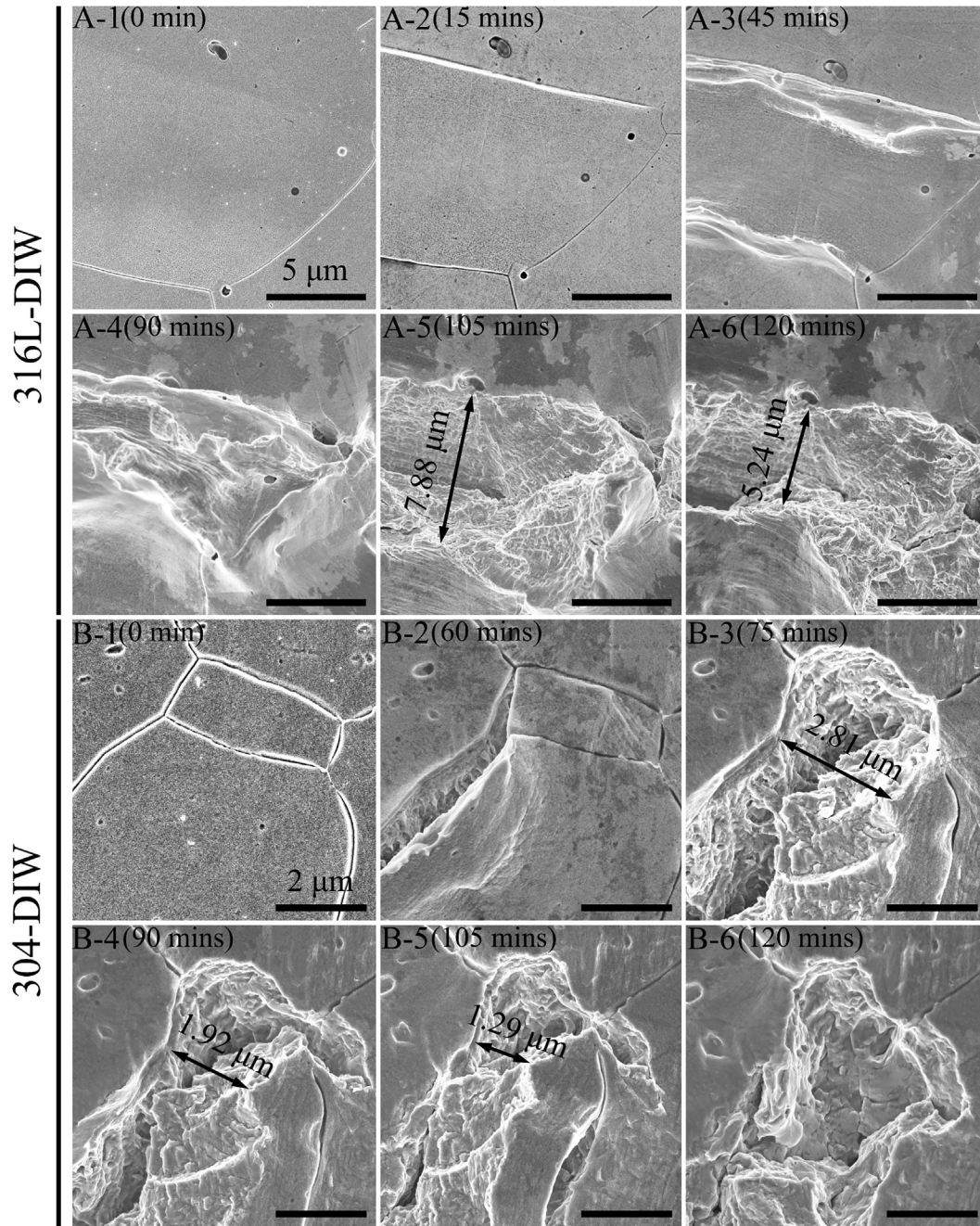


**Fig. 5.** *In-situ* observation showing the formation and the evolution of the cavitation crater in 316L SS and 304 SS during cavitation erosion in DIW.

Thus, the pre-existing pores in the austenitic stainless steels are not the initiation point of cavitation erosion. However, many studies reported that cavitation erosion preferentially occurred at the pre-existing pores [29,61–63], contrary to the results observed in this study. Materials (such as high-velocity oxy-fuel (HVOF)-sprayed WC-10Co4Cr, Co-based, Cr<sub>3</sub>C<sub>2</sub>-NiCr, and Fe-based amorphous/nanocrystalline coatings) have Vickers hardness up to 500 [29,61–63], which are brittle, and thus it is difficult to fill the pre-existing pores by deformation. The pores are the nucleation sites of cavitation bubbles [42]. As a result, the pre-existing pores

in the brittle coatings expand after a period of cavitation erosion, forming the initial site of cavitation erosion. However, for the austenitic stainless steels, when the grains around the pore were affected by the cavitation shock wave and/or microjets, they expanded towards the pore to absorb energy, resulting in the continuous shrinkage of the pore, which could be attributed to the low hardness and ductility of austenitic stainless steels. Fig. 8E shows a simulation that exhibits the microstructure evolution of the pre-existing pore of austenitic stainless steels subjected to cavitation erosion.

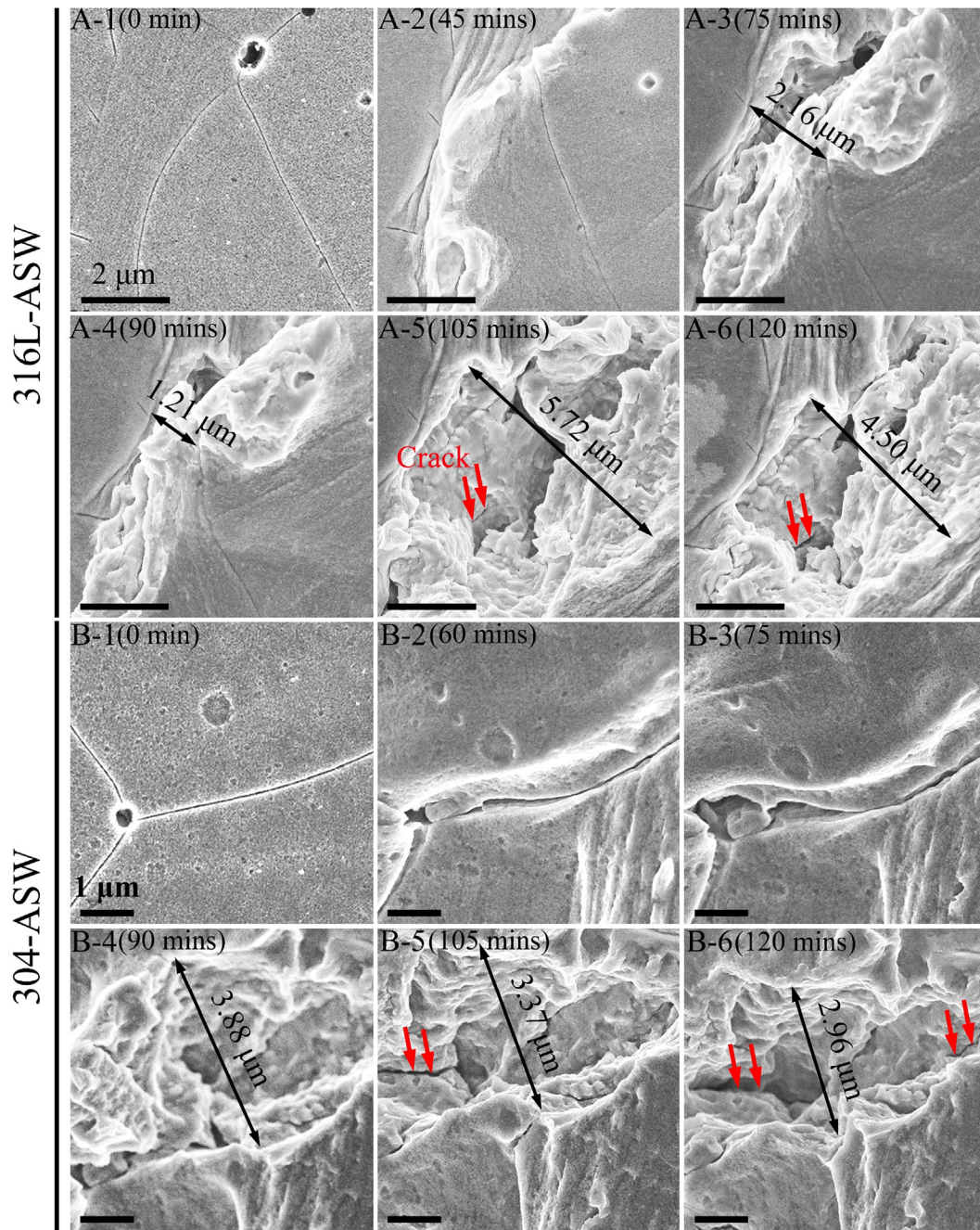


**Fig. 6.** *In-situ* observation showing the formation and the evolution of the cavitation crater in 316L SS and 304 SS during cavitation erosion in ASW (red arrow: cracks). (For interpretation of the references to colour in this figure legend, the reader is referred to the web version of this article.)

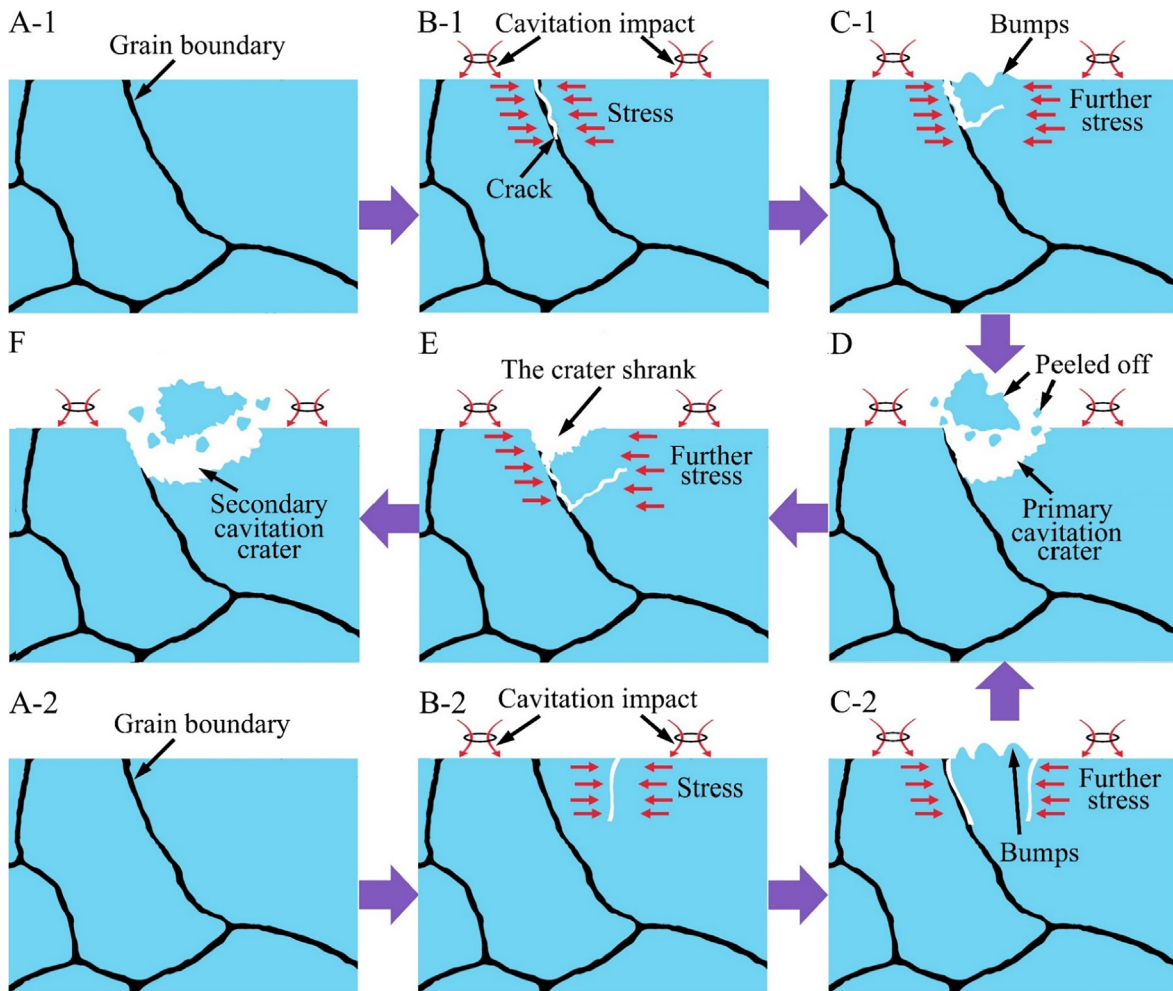


Fig. 7. Schematics demonstrating the formation and the evolution progress of the cavitation crater during cavitation erosion.

#### 4. Conclusions

This study investigated the failure mechanisms of the 316L SS and 304 SS subjected to ultrasonic cavitation erosion in DIW and ASW. The following conclusions could be drawn:

- (1) A corrosive medium, such as seawater, induces tensile stress release on the surface of austenitic stainless steels, resulting in more cracks on the surface of austenitic stainless steels and more sites for developing cavitation erosion craters. Thus, the acceleration of cavitation erosion can be attributed to corrosion.
- (2) After 45 min of cavitation erosion, the 304 SS undergoes a stress-induced martensitic transformation during cavitation erosion in both DIW and ASW, but the 316L SS does not.
- (3) During cavitation erosion, the inconsistent movement between grains causes the accumulation of stress in the grain and/or at the grain boundary. When the stress reaches

the plastic limit of the austenitic stainless steels, cracks form in the grain and/or at the grain boundary, which are the initiation points of cavitation erosion.

- (4) Continuously accumulated stress results in forming a primary cavitation crater. However, instead of expanding directly, the size of the primary cavitation crater will first decrease and then increase. Further exposure to cavitation erosion can cause the grains at/near the primary crater to be peeled off, resulting in the formation of the secondary cavitation crater.
- (5) Pre-existing pores on austenitic stainless steels are not the initiation points of cavitation erosion either in ASW or DIW, opposite to what has been reported in the other studies.

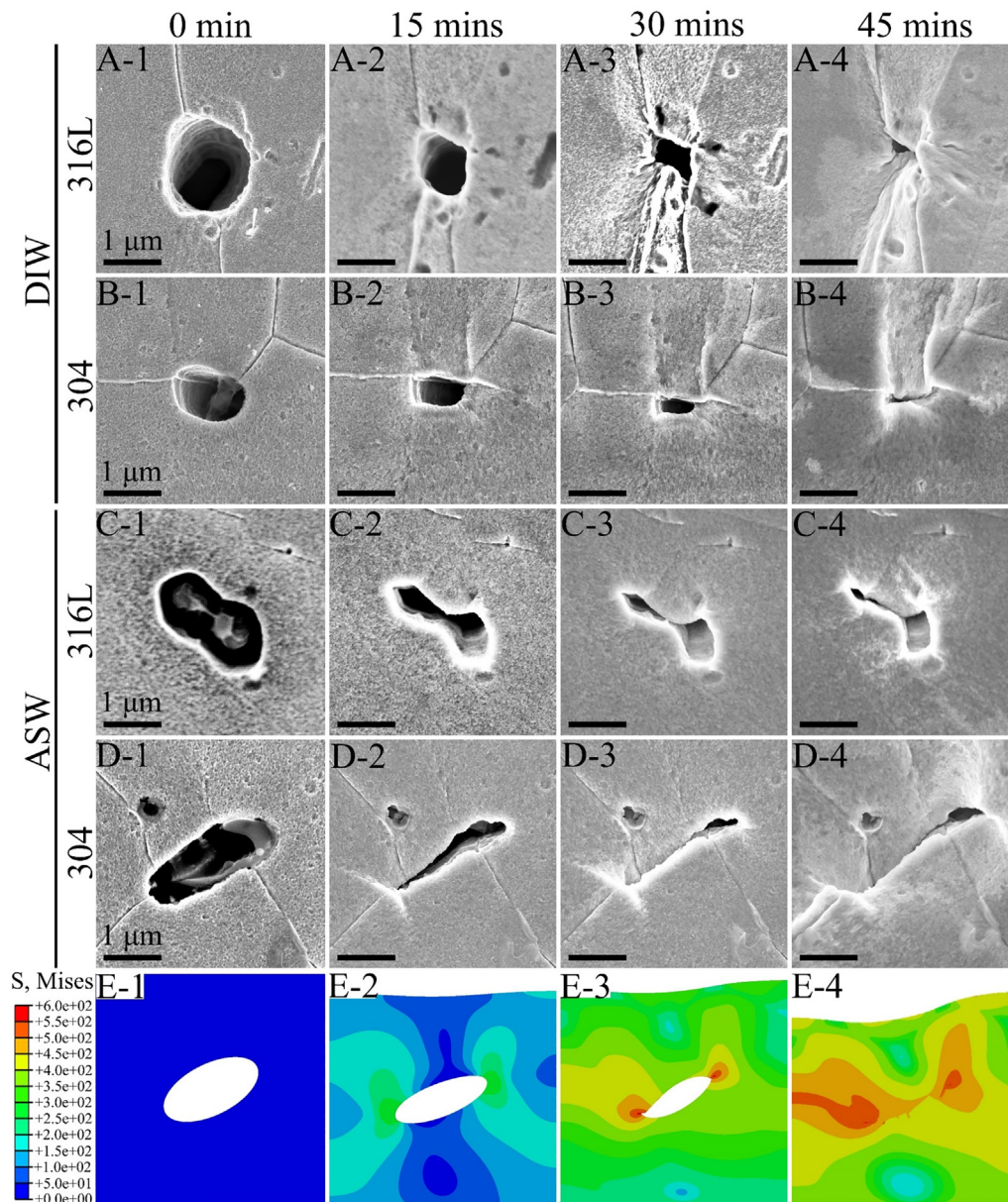


**Fig. 8.** (A–D) *In-situ* SEM observation of the pre-existing pore of the 316L SS and 304 SS during cavitation erosion in DIW and ASW, and (E) Finite element simulation of stress distribution around pre-existing pore during cavitation erosion.

### Declaration of Competing Interest

The authors declare that they have no known competing financial interests or personal relationships that could have appeared to influence the work reported in this paper.

### Acknowledgements

This work was supported by the Zhejiang Provincial Natural Science Foundation of China (grant # LZ22E090001), Ningbo 3315 Talents Program (grant # 2020A-29-G), Chinese Academy of Sciences President's International Fellowship Initiative (grant # 2020VEA0005), and a Natural Sciences and Engineering Research Council of Canada Discovery Grant (grant # NSERC RGPIN-2018-04298).

### Appendix A. Supplementary material

Supplementary data to this article can be found online at <https://doi.org/10.1016/j.matdes.2021.110314>.

### References

- [1] Z. Wang, B. Zhang, Cavitation erosion behavior of high-nitrogen austenitic stainless steel: Effect and design of grain-boundary characteristics, *Mater. Design* 201 (2021) 109496, <https://doi.org/10.1016/j.matdes.2021.109496>.
- [2] E. Hao, X. Liu, Y. An, H. Zhou, F. Yan, The coupling effect of immersion corrosion and cavitation erosion of NiCoCrAlYTa coatings in artificial seawater, *Corros. Sci.* 169 (2020) 108635, <https://doi.org/10.1016/j.corsci.2020.108635>.
- [3] S.L. Jiang, Y.G. Zheng, Z.M. Yao, Cavitation erosion behaviour of 20SiMn low alloy steel in  $\text{Na}_2\text{SO}_4$  and  $\text{NaHCO}_3$  solutions, *Corros. Sci.* 48 (9) (2006) 2614–2632, <https://doi.org/10.1016/j.corsci.2005.09.004>.
- [4] L. Qiao, Y. Wu, S. Hong, J. Cheng, Ultrasonic cavitation erosion mechanism and mathematical model of HVOF sprayed Fe-based amorphous/nanocrystalline coatings, *Ultrason. Sonochem.* 52 (2019) 142–149, <https://doi.org/10.1016/j.ultsonch.2018.11.010>.

- [5] W. Deng, G. Hou, S. Li, J. Han, X. Zhao, X. Liu, Y. An, H. Zhou, J. Chen, A new methodology to prepare ceramic-organic composite coatings with good cavitation erosion resistance, *Ultrason. Sonochem.* 44 (2018) 115–119, <https://doi.org/10.1016/j.ultsonch.2018.02.018>.
- [6] A. Abdullah, M. Malaki, E. Baghizadeh, On the impact of ultrasonic cavitation bubbles, *P. I. Mech. Eng. C-J. MEC* 226 (3) (2012) 681–694, <https://doi.org/10.1177/0954406211414769>.
- [7] L.M. Zhang, Z.X. Li, J.X. Hu, A.L. Ma, S. Zhang, E.F. Daniel, A.J. Umoh, H.X. Hu, Y.G. Zheng, Understanding the roles of deformation-induced martensite of 304 stainless steel in different stages of cavitation erosion, *Tribol. Int.* 155 (2021) 106752, <https://doi.org/10.1016/j.triboint.2020.106752>.
- [8] L.L. Santos, R.P. Cardoso, S.F. Brunatto, Direct correlation between martensitic transformation and incubation-acceleration transition in solution-treated AISI 304 austenitic stainless steel cavitation, *Wear* 462–463 (2020) 203522, <https://doi.org/10.1016/j.wear.2020.203522>.
- [9] R.Y. Ting, Polymer effects on microjet impact and cavitation erosion, *Nature* 262 (1976) 572–573, <https://doi.org/10.1038/262572a0>.
- [10] A. Crespo, F. Castro, F. Manuel, J. Hernandez, Dynamics of an elongated bubble during collapse, *J. Fluid. Eng.-T. ASME* 112 (1990) 232–237, <https://doi.org/10.1115/1.2909393>.
- [11] S.A. Karrab, M.A. Doheim, M.S. Aboraia, S.M. Ahmed, Study of cavitation erosion pits on 1045 carbon steel surface in corrosive waters, *J. Tribol.-T. ASME* 134 (2012), <https://doi.org/10.1115/1.4005646> 011602.
- [12] R. Bugala, M. Szkodo, The effect of cavitation loading spectrum on microhardness in an Al alloy AlMg<sub>2</sub>Mn, *Wear* 233 (1999) 75–78, [https://doi.org/10.1016/S0043-1648\(99\)00198-2](https://doi.org/10.1016/S0043-1648(99)00198-2).
- [13] A. Karimi, Cavitation erosion of austenitic stainless steel and effect of boron and nitrogen ion implantation, *Acta Metall.* 37 (4) (1989) 1079–1088, [https://doi.org/10.1016/0001-6160\(89\)90104-1](https://doi.org/10.1016/0001-6160(89)90104-1).
- [14] G.L. Chahine, J. Franc, A. Karimi, Cavitation and cavitation erosion, in: K. Kim, G. Chahine, J. Franc, A. Karimi (Eds.), *Advanced experimental and numerical techniques for cavitation erosion prediction*, Springer, Germany, 2014, pp. 3–20.
- [15] A. Krella, Influence of cavitation intensity on X6CrNiTi18-10 stainless steel performance in the incubation period, *Wear* 258 (11–12) (2005) 1723–1731, <https://doi.org/10.1016/j.wear.2004.11.025>.
- [16] A.K. Krella, Degradation of AlMg<sub>2</sub> aluminium alloy caused by cavitation - An effect of cavitation intensity, *Mater. Charact.* 130 (2017) 219–229, <https://doi.org/10.1016/j.matchar.2017.06.015>.
- [17] M.C. Park, K.N. Kim, G.S. Shin, J.Y. Yun, M.H. Shin, S.J. Kim, Effects of Ni and Mn on the cavitation erosion resistance of Fe-Cr-C-Ni/Mn austenitic alloys, *Tribol. Lett.* 52 (3) (2013) 477–484, <https://doi.org/10.1007/s11249-013-0231-x>.
- [18] D. Drodzdz, R.K. Wunderlich, H.-J. Fecht, Cavitation erosion behaviour of Zr-based bulk metallic glasses, *Wear* 262 (1–2) (2007) 176–183, <https://doi.org/10.1016/j.wear.2006.04.008>.
- [19] W. Liu, Y.G. Zheng, C.S. Liu, Z.M. Yao, W. Ke, Cavitation erosion behavior of Cr-Mn-N stainless steels in comparison with 0Cr13Ni5Mo stainless steel, *Wear* 254 (7–8) (2003) 713–722, [https://doi.org/10.1016/S0043-1648\(03\)00128-5](https://doi.org/10.1016/S0043-1648(03)00128-5).
- [20] J.F. dos Santos, C.M. Garzón, A.P. Tschiptschin, Improvement of the cavitation erosion resistance of an AISI 304L austenitic stainless steel by high temperature gas nitriding, *Mater. Sci. Eng., A* 382 (1–2) (2004) 378–386, <https://doi.org/10.1016/j.msea.2004.05.003>.
- [21] A.K. Krella, A. Maurin, Z. Krzemianowski, Degradation of Armco iron caused by cavitation: Part II - Correlation with stress analysis, *Eng. Fail. Anal.* 128 (2021) 105621, <https://doi.org/10.1016/j.engfailanal.2021.105621>.
- [22] A.K. Krella, Cavitation erosion of monolayer PVD coatings - An influence of deposition technique on the degradation process, *Wear* 478–479 (2021) 203762, <https://doi.org/10.1016/j.wear.2021.203762>.
- [23] X.J. Wang, K. Wu, W.X. Huang, H.F. Zhang, M.Y. Zheng, D.L. Peng, Study on fracture behavior of particulate reinforced magnesium matrix composite using *in situ* SEM, *Compos. Sci. Technol.* 67 (11–12) (2007) 2253–2260, <https://doi.org/10.1016/j.compscitech.2007.01.022>.
- [24] G. Zhu, S. Li, R. Wang, D. Wang, A. Dong, D. Shu, L. Zhang, B. Sun, *In-situ* SEM investigation on fracture behavior of GTD222 superalloy during tensile process at 760°C, *J. Mater. Res. Technol.* 9 (2020) 15185–15190, <https://doi.org/10.1016/j.jmrt.2020.11.004>.
- [25] Z. Wang, W. Wu, G. Qian, L. Sun, X. Li, J.A.F.O. Correia, *In-situ* SEM investigation on fatigue behaviors of additive manufactured Al-Si10-Mg alloy at elevated temperature, *Eng. Fract. Mech.* 214 (2019) 149–163, <https://doi.org/10.1016/j.engfracmech.2019.03.040>.
- [26] H. Song, C. Liu, H. Zhang, J. Du, X. Yang, S.B. Leen, *In-situ* SEM study of fatigue micro-crack initiation and propagation behavior in pre-corroded AA7075-T7651, *Int. J. Fatigue* 137 (2020) 105655, <https://doi.org/10.1016/j.ijfatigue.2020.105655>.
- [27] H. Shao, Y. Zhao, P. Ge, W. Zeng, *In-situ* SEM observations of tensile deformation of the lamellar microstructure in TC21 titanium alloy, *Mater. Sci. Eng., A* 559 559 (2013) 515–519, <https://doi.org/10.1016/j.msea.2012.08.134>.
- [28] F. Liu, H. Zhao, R. Yang, F. Sun, Crack propagation behavior of die-cast AlSiMgMn alloys with *in-situ* SEM observation and finite element simulation, *Mater. Today Commun.* 19 (2019) 114–123, <https://doi.org/10.1016/j.mtcomm.2019.01.009>.
- [29] H. Zhang, X. Chen, Y. Gong, Y.e. Tian, A. McDonald, H. Li, *In-situ* SEM observations of ultrasonic cavitation erosion behavior of HVOF-sprayed coatings, *Ultrason. Sonochem.* 60 (2020) 104760, <https://doi.org/10.1016/j.ultsonch.2019.104760>.
- [30] P.-H. Huang, L.-L. Shih, H.-M. Lin, C.-I. Chu, C.-S. Chou, Novel approach to investment casting of heat-resistant steel turbine blades for aircraft engines, *Int. J. Adv. Manuf. Tech.* 104 (5–8) (2019) 2911–2923, <https://doi.org/10.1007/s00170-019-04178-z>.
- [31] D.F. Susan, T.B. Crenshaw, J.S. Gearhart, The effects of casting porosity on the tensile behavior of investment cast 17-4PH stainless steel, *J. Mater. Eng. Perform.* 24 (8) (2015) 2917–2924, <https://doi.org/10.1007/s11665-015-1594-y>.
- [32] P. Haušild, C. Berdin, P. Bompard, N. Verdère, piping, Ductile fracture of duplex stainless steel with casting defects, *Int. J. Pres. Ves. Pip.* 78 (9) (2001) 607–616, [https://doi.org/10.1016/S0308-0161\(01\)00069-2](https://doi.org/10.1016/S0308-0161(01)00069-2).
- [33] D1141-98, Standard practice for the preparation of substitute ocean water, PA: ASTM International, West Conshohocken, 2013. <https://doi.org/10.1520/D1141-98R13>.
- [34] G. Vander Voort, G.M. Lucas, E.P. Manilova, Metallography and microstructures of stainless steels and maraging steels, in: G. Vander Voort (Ed.) *ASM Handbook*, ASM International, USA, 2004, pp. 670–700.
- [35] R. Johnson, W.K. Cook, A constitutive model and data for metals subjected to large strains high strain rates and high temperatures, in: *The 7th International Symposium on Ballistics*, Netherlands (1983) 541–547.
- [36] R. Abbaschian, L. Abbaschian, R.E. ReedHill, *Physical metallurgy principles*, in: F. Edtm (Ed.) *Characterization Techniques*, Cengage Learning, United States of America, 2009, pp. 29–61.
- [37] S. Feng, Y. Yang, J. Wang, Y. Wang, X. Zhou, Improved mechanical properties and fracture mechanism of C/C composites with salt treatment monitored by synchrotron-based *in-situ* tensile XRD, *Compos. Part B-Eng.* 199 (2020) 108274, <https://doi.org/10.1016/j.compositesb.2020.108274>.
- [38] R. Kwesi Nutor, X. Xu, X. Fan, X. He, X. Lu, Y. Fang, Effects of applying tensile stress during annealing on the GMI and induced anisotropy of Fe-Cu-Nb-Si-B alloys, *J. Magn. Magn. Mater.* 471 (2019) 544–548, <https://doi.org/10.1016/j.jmmm.2018.09.061>.
- [39] F. Delaunois, A. Tshimombo, V. Stanciu, V. Vitry, Monitoring of chloride stress corrosion cracking of austenitic stainless steel: identification of the phases of the corrosion process and use of a modified accelerated test, *Corros. Sci.* 110 (2016) 273–283, <https://doi.org/10.1016/j.corsci.2016.04.038>.
- [40] M. Ananda Rao, R. Sekhar Babu, M.V. Pavan Kumar, Stress corrosion cracking failure of a SS 316L high pressure heater tube, *Eng. Fail. Anal.* 90 (2018) 14–22, <https://doi.org/10.1016/j.engfailanal.2018.03.013>.
- [41] Y.Z. Huang, J.M. Titchmarsh, TEM investigation of intergranular stress corrosion cracking for 316 stainless steel in PWR environment, *Acta Mater.* 54 (3) (2006) 635–641, <https://doi.org/10.1016/j.actamat.2005.10.011>.
- [42] Y. Wang, J. Liu, N. Kang, G. Darut, T. Poirier, J. Stella, H. Liao, M.P. Planche, Cavitation erosion of plasma-sprayed CoMoCrSi coatings, *Tribol. Int.* 102 (2016) 429–435, <https://doi.org/10.1016/j.triboint.2016.06.014>.
- [43] L. Bai, W. Xu, F. Zhang, N. Li, Y. Zhang, D. Huang, Cavitation characteristics of pit structure in ultrasonic field, *Sci. China Ser. E* 52 (7) (2009) 1974–1980, <https://doi.org/10.1007/s11431-009-0132-2>.
- [44] Y. Liu, B. Hu, X. Lan, P. Fu, Micromagnetic characteristic changes and mechanism induced by plastic deformation of 304 austenitic stainless steel, *Mater. Today Commun.* 27 (2021) 102188, <https://doi.org/10.1016/j.mtcomm.2021.102188>.
- [45] A. Kundu, D.P. Field, P. Chandra Chakraborti, Effect of strain and strain rate on the development of deformation heterogeneity during tensile deformation of a solution annealed 304 LN austenitic stainless steel: An EBSD study, *Mater. Sci. Eng., A* 773 (2020) 138854, <https://doi.org/10.1016/j.msea.2019.138854>.
- [46] Y. Izuta, K. Prasad, A. Ito, M. Tanaka, S. Torizuka, Transmission X ray diffraction characterization of deformation induced martensite in 301 and 304 stainless steels rolled at 77K: Role of grain size, *Mater. Sci. Eng., A* 794 794 (2020) 139984, <https://doi.org/10.1016/j.msea.2020.139984>.
- [47] J. Talonen, H. Hänninen, Formation of shear bands and strain-induced martensite during plastic deformation of metastable austenitic stainless steels, *Acta Mater.* 55 (18) (2007) 6108–6118, <https://doi.org/10.1016/j.actamat.2007.07.015>.
- [48] L. Ye, X. Zhu, X. Wei, S. Wu, Damage characteristics and surface description of near-wall materials subjected to ultrasonic cavitation, *Ultrason. Sonochem.* 67 (2020) 105175, <https://doi.org/10.1016/j.ultsonch.2020.105175>.
- [49] L. Ye, X. Zhu, Y. He, T. Song, W. Hu, Surface strengthening and grain refinement of AZ31B magnesium alloy by ultrasonic cavitation modification, *Chinese J. Aeronaut.* 34 (4) (2021) 508–517, <https://doi.org/10.1016/j.cja.2020.08.043>.
- [50] J.R.C. Guimarães, C. Rios Maria, The hardness of martensite-austenite mixtures in Fe-31.9% Ni-0.02% C, *Mater. Sci. Eng.* 43 (1) (1980) 55–58, [https://doi.org/10.1016/0025-5416\(80\)90207-4](https://doi.org/10.1016/0025-5416(80)90207-4).
- [51] J. Mola, M. Ren, On the hardness of high carbon ferrous martensite, *IOP Conf. Ser.: Mater. Sci. Eng.* 373 (2018) 012004, <https://doi.org/10.1088/1757-899X/373/1/012004>.
- [52] A.K. Krella, A. Krupa, Effect of cavitation intensity on degradation of X6CrNiTi18-10 stainless steel, *Wear* 408–409 (2018) 180–189, <https://doi.org/10.1016/j.wear.2018.05.015>.
- [53] G. Hou, Y.i. Ren, X. Zhang, F. Dong, Y. An, X. Zhao, H. Zhou, J. Chen, Cavitation erosion mechanisms in Co-based coatings exposed to seawater, *Ultrason. Sonochem.* 60 (2020) 104799, <https://doi.org/10.1016/j.ultsonch.2019.104799>.
- [54] Z. Wang, A. Seyeux, S. Zanna, V. Maurice, P. Marcus, Chloride-induced alterations of the passive film on 316L stainless steel and blocking effect of pre-passivation, *Electrochim. Acta* 329 (2020) 135159, <https://doi.org/10.1016/j.electacta.2019.135159>.

- [55] C.T. Liu, J.K. Wu, Influence of pH on the passivation behavior of 254SMO stainless steel in 3.5% NaCl solution, *Corros. Sci.* 49 (5) (2007) 2198–2209, <https://doi.org/10.1016/j.corsci.2006.10.032>.
- [56] S. Hattori, N. Mikami, Cavitation erosion resistance of stellite alloy weld overlays, *Wear* 267 (11) (2009) 1954–1960, <https://doi.org/10.1016/j.wear.2009.05.007>.
- [57] G. Gao, Z. Zhang, Cavitation erosion behavior of 316L stainless steel, *Tribol. Lett.* 67 (2019) 112, <https://doi.org/10.1007/s11249-019-1225-0>.
- [58] J. Li, R. Chen, Y. Ma, W. Ke, Characterization and prediction of microporosity defect in sand cast WE54 alloy castings, *J. Mater. Sci. Technol.* 30 (10) (2014) 991–997, <https://doi.org/10.1016/j.jmst.2014.03.011>.
- [59] A. Brueckner, M. Luetje, M. Wicke, I. Bacaicoa, A. Geisert, M. Fehlbier, On the role of internal defects in the fatigue damage process of a cast Al-Si-Cu alloy, *Int. J. Fatigue* 116 (2018) 562–571, <https://doi.org/10.1016/j.ijfatigue.2018.07.012>.
- [60] L. Wang, N. Limodin, A. El Bartali, J.-F. Witz, R. Seghir, J.-Y. Buffiere, E. Charkaluk, Influence of pores on crack initiation in monotonic tensile and cyclic loadings in lost foam casting A319 alloy by using 3D *in-situ* analysis, *Mater. Sci. Eng., A* 673 673 (2016) 362–372, <https://doi.org/10.1016/j.msea.2016.07.036>.
- [61] R.K. Kumar, M. Kamaraj, S. Seetharamu, T. Pramod, P. Sampathkumaran, Effect of spray particle velocity on cavitation erosion resistance characteristics of HVOF and HVOF processed 86WC-10Co4Cr hydro turbine coatings, *J. Therm. Spray Technol.* 25 (6) (2016) 1217–1230, <https://doi.org/10.1007/s11666-016-0427-3>.
- [62] G. Taillon, F. Pougoum, S. Lavigne, L. Ton-That, R. Schulz, E. Bousser, S. Savoie, L. Martinu, J.-E. Klemberg-Sapieha, Cavitation erosion mechanisms in stainless steels and in composite metal-ceramic HVOF coatings, *Wear* 364–365 (2016) 201–210.
- [63] C. Harges, F. Pöhl, A. Röttger, M. Thiele, W. Theisen, C. Esen, Cavitation erosion resistance of 316L austenitic steel processed by selective laser melting (SLM), *Addit. Manuf.* 29 (2019) 100786, <https://doi.org/10.1016/j.addma.2019.100786>.